

# Bayesian inference of PolII dynamics over the exclusion process.

Massimo Cavallaro,<sup>1,2,3,\*</sup> Yuexuan Wang,<sup>4</sup> Daniel Hebenstreit,<sup>2</sup> and Ritabrata Dutta<sup>5</sup>

<sup>1</sup>*Mathematics Institute, University of Warwick, Coventry, UK*

<sup>2</sup>*School of Life Sciences, University of Warwick, Coventry, UK*

<sup>3</sup>*Zeeman Institute for Systems Biology and Infectious Disease Epidemiology Research,  
University of Warwick, Coventry, UK*

<sup>4</sup>*Institute of Applied Statistics, Johannes Kepler Universität, Linz, Austria*

<sup>5</sup>*Department of Statistics, University of Warwick, Coventry, UK*

## Abstract

Transcription is a complex phenomenon that permits the conversion of genetic information into phenotype by means of an enzyme called PolII, which erratically moves along and scans the DNA template. We perform Bayesian inference over a paradigmatic mechanistic model of non-equilibrium statistical physics, i.e., the asymmetric exclusion processes in the hydrodynamic limit, assuming a Gaussian process prior for the PolII progression rate as a latent variable. Our framework allows us to infer the speed of PolIIs during transcription given their spatial distribution, whilst avoiding the explicit inversion of the system's dynamics. The results, which show processing rates strongly varying with genomic position and minor role of traffic-like congestion, may have implications for the understanding of gene expression.

---

\* m.cavallaro@warwick.ac.uk

## I. INTRODUCTION

DNA is a long polymeric molecule that encodes information as a sequence of nucleotides (Nts). Turning this information into a phenotype is a complex phenomenon hinged upon transcription, the molecular process in which particular segments of DNA (i.e., the genes) are scanned and their information is copied into mRNA by the enzyme RNA polymerase II (PolII). The transcription itself consists of several steps which can be differentially regulated to alter the timing and the output of the mRNA production [1, 2].

The transcription can also be seen as a non-equilibrium process, where the PolIIs are being transported as particles on a one dimensional lattice, the lattice being the DNA template which the PolIIs bind to. We can further consider this process having left and right boundaries, representing the transcription start site (TSS) and the transcription end site (TES), respectively (Fig. 1 A). Within the gene body, the PolIIs erratically travel along the template and their abrupt slowing down in certain genomic regions is known as *pausing* dynamics [3, 4]. While the pausing is an essential part of the transcriptional machinery and contributes to the regulation of genes' expression levels, a comprehensive quantitative understanding of its dynamics is still missing [5, 6].

We present a modelling framework to help understand gene regulation and quantitatively study the pausing dynamics given real-world data. In literature, a number of different mechanistic models have been introduced to elucidate transcription, starting from the simple telegraph model [7] to more complicated multi-state models that account for many interactions [8–11], with each model reflecting determinate aspects of the whole biological system complexity. Here we are primarily interested in the pausing and employ a generalisation of a paradigmatic model of particle transport, the asymmetric simple exclusion process (ASEP, [12]) in the hydrodynamic limit [13]. The ASEP is a class of models of particles on a one-dimensional lattice, whose behaviour is chiefly determined by the rates at which the particles hop on the lattice. More specifically we require the rate profile function, which we refer to as  $\tilde{p}$ , to be spatially varying yet smooth as in reference [14], see also [15], thus making it possible to model this function by a Gaussian process (GP) [16]. Noticing the analogy between the PolII transport in the gene body and the particle hopping in the exclusion process, learning  $\tilde{p}$  allows the study of the pausing dynamics in a gene. Importantly, we provide an inferential scheme to learn this rate function by Bayesian inference given real

molecular-biology data, assuming a prior on the profile function induced by a GP prior on a latent variable. In other words, integrating the dynamics defined by the rate  $\tilde{p}$  generates transient time-course density profiles; we estimate  $\tilde{p}$  given observed density profiles without explicitly inverting the system’s dynamics. Other models of PolIII dynamics also leverage GPs for inference from biological data, with GPs representing transcriptional activity over time [17, 18]. In contrast, the GP here describes a function of genomic position, with its minima corresponding to pausing regions. Due to its generality, our framework can be deployed to estimate the rate profiles of any one-dimensional transport problem.

The manuscript is organised as follows. Section II A describes the biology of pausing and the next-generation sequencing (NGS) data types which are available to study it. Section II B and II C, respectively, discuss the asymmetric simple exclusion process as a mathematical model for transcription with pausing and a Bayesian inferential framework for model fitting. We present the results in section III and conclude with a discussion in section IV.

## II. MODEL DEFINITION

### A. Biological processes and data

The enzyme PolIII has a central role in the biology of transcription. In order to catalyse synthesis of the mRNA, it binds to the DNA upstream the TSS, initiates the mRNA synthesis, and then traverses the DNA downstream (elongation) until it pauses at a certain gene location, ready to respond to a developmental or environmental signal that instructs to resume the elongation. The process terminates when the PolIII reaches the TES and the transcribed mRNA is released. As a result of these steps, the output is modulated in both timing and intensity. However, many details, such as the pausing, are not well understood [5]. The presence of transcriptional pausing is revealed by several assays based on NGS, which is widely used in molecular biology to study molecules involved in genic processes. In the PolIII *ChIP-seq* assay, PolIII-bound DNA is isolated by chromatin immunoprecipitation with a PolIII antibody and is then subject to high-throughput sequencing. This provides a genome-wide view of the PolIII binding sites for all forms of PolIII, including both those poised or transcriptionally engaged and those which are bound to DNA and static. For each genomic position, PolIII ChIP-seq returns a signal when the position is found occupied

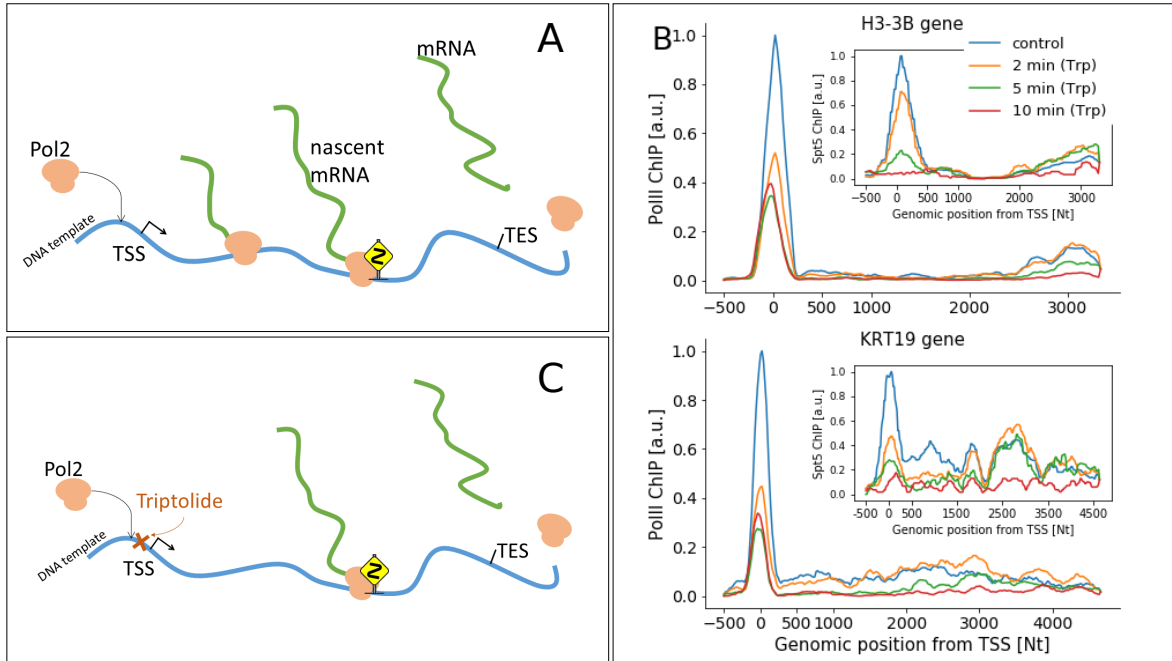


FIG. 1. Biological processes and data. A) Simplified diagram of mRNA synthesis. PolIII molecules bind to the DNA upstream of transcription start site (TSS) and moves downstream towards the transcription end site (TES), where it is released along with the synthesized mRNA. Obstacles along the gene (represented by a dangerous bend sign,  $\diamond$ ) slow down or interrupt this process. B) ChIP-seq experiments yield the relative abundance of PolIII at each genomic position, here illustrated for H3-3B (top) and KR19 genes (bottom); insets show the Spt5-bound PolIII abundances for the same genes. C) In the presence of triptolide, transport is blocked upstream of TSS, while transcriptional engaged PolII are allowed to complete elongation; this is reflected in the ChIP-seq profiles obtained 2, 5, and 10 minutes after treatment (also in B).

by a polymerase.

For this study, we binned ChIP-seq reads from genomic ranges of selected genes (*Materials and Methods*) into 20-Nt bins, thus yielding coarse-grained read profiles (which we refer to as  $y$ ) such as those illustrated in Fig. 1 B. The number of these reads at a position  $x$  is proportional to the occupation probability  $\rho(x)$ . The proportionality factor, which depends on the number of cells used in the experiment and on further signal amplification intrinsic to the sequencing procedure, cannot be directly accessed with precision and is only known with substantial uncertainty [19].

Other methods available to study the pausing include but are not limited to *NET-*

*seq*, where nascent mRNA chunks associated with immunoprecipitated PolII complexes are isolated and sequenced [20], *GRO-seq*, where RNAs recently transcribed only by transcriptionally-engaged PolIIs are sequenced [21], and *PRO-seq*, which is similar to GRO-seq but reaches single-nucleotide resolution [22]. The evidences of PolII transport are particularly clear in time-course experiments, where sequencing data are collected over time following a perturbation. As an example, time-variant PRO-seq has been suggested to estimate pausing times in key peak regions [23]. A classical way to perturb these molecular dynamics is inhibiting the initiation by treating the cells with triptolide (Trp) [24, 25]. This permits the PolII already engaged in transcription to progress further downstream the gene while new PolIIs are prevented to attach, thus freeing upstream genomic regions as the run-on time progresses (Fig. 1 C). Our approach consists of using the read profiles  $y$  as functions of  $x$ , collected at fixed run-on times  $t_1$ ,  $t_2$ ,  $t_3$ , and  $t_4$  after treatment, to infer the dynamics. While Trp inhibits new initiation, poised PolII upstream the TSS can still pass through it, enter the gene template, and perform elongation immediately after Trp treatment [24, 25]. To account for this, we also perform inference over Spt5 ChIP-seq data, where the poised polymerases are masked while those bound are detected [25].

These types of experiments reveal the presence of a flux of PolIIs, which is the signature of the non-equilibrium physics involved in the elongation process. The profile  $y^*$  observed prior to the treatment corresponds to a non-equilibrium stationary state (NESS). Disrupting initiation with Trp yields a transient state, which evolves from  $y^*$  until it settles down to a new NESS.

## B. Mathematical model

The transport of particles on a one dimensional lattice is a well-studied problem in mathematics and physics. Its basic features are captured by the asymmetric simple exclusion process (ASEP) [12], which defines the stochastic dynamics of interacting particles on a discrete lattice, which we take here to be a one-dimensional chain with open boundary conditions. Let the total number of lattice sites be  $N$ . The state of each site  $i$ ,  $1 \leq i \leq N$ , is characterized by the occupation number  $n_i$  such that  $n_i = 0$  if the site is empty and  $n_i = 1$  if it is occupied by a particle. The evolution proceeds in continuous time. A particle on site  $i < N$  hops rightward into the site  $i + 1$  with rate  $p_i$ , the transition being successful

only if the site  $i + 1$  is empty. Similarly, a particle on site  $i > 1$  hops leftward into  $i - 1$  with rate  $q_i$ , if the site  $i - 1$  is empty. Further, particles on the left (right) boundary site  $i = 1$  ( $i = N$ ) leave the lattice at rate  $q_0$  ( $p_N$ ), while particles are injected in the same boundary site at rate  $p_0$  ( $q_N$ ) if the site is empty. The constraint that a jump can occur only if the target is empty prevents the accumulation of more than one particle on a site and is generically referred to as the exclusion rule. This rule allows particle collision, which causes congestion when the particle density is sufficiently high and permits phase transitions between a low density, high density, and a maximum current phase even if the systems is one dimensional [26]. Interestingly, based on theoretical considerations, it has been suggested that traffic-like congestion of PolIIs is important in transcription [27–29].

While the ASEP was originally proposed to model biopolymerization on DNA [30], this and related models have been applied to diverse problems, e.g., protein translation [31–33], molecular motors [34], pedestrian and vehicle traffic [35]. Applications to transcription incorporating disordered dynamics and obstacles (e.g., [36, 37]) were also proposed. ASEP’s theoretical appeal is due to its analytical results representative of a large class of models [38, 39] and a convenient mean-field treatment that yields the exact stationary solution [40]. In the context of transcription, particles entering site 1, moving along the chain, and exiting from site  $N$  correspond to initiation, elongation, and termination, respectively. In our setting, the lowest values of  $p_i$  correspond to obstacles which hinder the movement across pausing sites in the gene.

The dynamics of the expected occupation of a single site  $i$  in the bulk are governed by the lattice continuity equation

$$\frac{d}{dt}\mathbb{E}(n_i(t)) = J^{\text{left}}(t) - J^{\text{right}}(t), \quad (1)$$

$0 < i < N$ , where  $\mathbb{E}$  denotes expectation value and  $J^{\text{left}}(t)$  and  $J^{\text{right}}(t)$  are the average flux of particles from site  $i - 1$  to site  $i$  and from site  $i$  to site  $i + 1$ , respectively. These are subject to the exclusion rule and therefore obey

$$\begin{aligned} J^{\text{left}}(t) &= p_{i-1}\mathbb{E}(n_{i-1}(t)(1 - n_i(t))) \\ &\quad - q_i\mathbb{E}(n_i(t)(1 - n_{i-1}(t))), \\ J^{\text{right}}(t) &= p_i\mathbb{E}(n_i(t)(1 - n_{i+1}(t))) \\ &\quad - q_{i+1}\mathbb{E}(n_{i+1}(t)(1 - n_i(t))). \end{aligned} \quad (2)$$

In order to exactly solve these dynamics, second-order moments such as  $\mathbb{E}(n_i(t)n_{i+1}(t))$  need to be known. Under independence assumption, these moments are factorised, which in our case amounts to replacing equations (1)–(2) with

$$\begin{aligned} \frac{d}{dt}\phi_i(t) &= p_{i-1}\phi_{i-1}(t)(1 - \phi_i(t)) - p_i\phi_i(t)(1 - \phi_{i+1}(t)) \\ &\quad + q_{i+1}\phi_{i+1}(t)(1 - \phi_i(t)) - q_i\phi_i(t)(1 - \phi_{i-1}(t)), \end{aligned} \quad (3)$$

where we used  $\phi_i(t) := \mathbb{E}(n_i(t))$  to lighten the notation. In other words, equations (3) define the so-called mean-field dynamics of the asymmetric exclusion process, which are known to approximate well the true dynamics in many contexts, predict crucial features such as dynamical phase-transitions, and ease mathematical treatment [26, 40, 41]. With open boundaries,

$$\begin{aligned} \frac{d}{dt}\phi_1(t) &= p_0(1 - \phi_1(t)) - p_1\phi_1(t)(1 - \phi_2(t)) \\ &\quad - q_0\phi_1(t) + q_1\phi_2(t)(1 - \phi_1(t)), \end{aligned} \quad (4)$$

$$\begin{aligned} \frac{d}{dt}\phi_N(t) &= p_{N-1}\phi_{N-1}(t)(1 - \phi_N(t)) - p_N\phi_N(t) \\ &\quad + q_N(1 - \phi_N(t)) - q_{N-1}\phi_N(1 - \phi_{N-1}). \end{aligned} \quad (5)$$

To match the available data that is coarse grained (Fig. 1 B), instead of considering particles individually we rely on their hydrodynamics description, which is obtained as follows. We assume Euler scaling with constant  $a$  and let  $a \rightarrow 0, N \rightarrow \infty$ , with  $L := Na$  held finite. We define the functions  $\varrho : \mathbb{R}^2 \rightarrow \mathbb{R}_0^+$ ,  $\tilde{p} : \mathbb{R} \rightarrow \mathbb{R}_0^+$ , and  $\tilde{q} : \mathbb{R} \rightarrow \mathbb{R}_0^+$  such that they are analytic and bounded on  $]0, L[ \times ]0, \infty[$ ,  $]0, L[$ , and  $]0, L[$ , respectively, and

$$\begin{aligned} \phi_i(t) &= \varrho((i-1)a, t), \\ p_i &= a\tilde{p}((i-1)a), \\ q_i &= a\tilde{q}((i-1)a), \end{aligned} \quad (6)$$

we further assume that the left and right jump rates satisfy  $\tilde{q}(x) = b\tilde{p}(x)$ ,  $\forall x \in [0, L]$ , with  $0 \leq b < 1$ , where  $b$  governs the relative strength of the non-equilibrium driving forces. The case  $b = 0$  corresponds to a *totally asymmetric exclusion process* (TASEP), while the limit case  $b = 1$  corresponds to the *symmetric exclusion process*. Intermediate values  $0 < b < 1$  correspond to settings where the particles can jump in both directions, but are driven rightwards in average, as expected in molecular biology [42, 43]. A continuum-limit

counterpart of equations (2), as derived in references [14, 15], is

$$J(x, t) = a\tilde{p}(x)\varrho(x - a/2, t)(1 - \varrho(x + a/2, t)) - a\tilde{q}(x)\varrho(x + a/2, t)(1 - \varrho(x - a/2, t)), \quad (7)$$

which, using first-order Taylor expansion, yields

$$J(x, t) \approx a(\tilde{p}(x) - \tilde{q}(x))\varrho(x, t)(1 - \varrho(x, t)) - \frac{a^2}{2}(\tilde{p}(x) + \tilde{q}(x))\frac{\partial}{\partial x}\varrho(x, t). \quad (8)$$

To lighten the mathematical notation, we define the two quantities

$$\begin{aligned} \lambda(x) &:= a(\tilde{p}(x) - \tilde{q}(x)) = a\tilde{p}(x)(1 - b), \\ \nu(x) &:= \frac{a^2}{2}(\tilde{p}(x) + \tilde{q}(x)) = \frac{a^2}{2}\tilde{p}(x)(1 + b); \end{aligned} \quad (9)$$

their ratio is constant in  $x$ , viz.,  $\nu(x)/\lambda(x) = a/2(1 + b)/(1 - b)$ , which equals  $a/2$  in the totally asymmetric case.

Substituting (8)–(9) into the continuity equation

$$\frac{\partial}{\partial t}\varrho(x, t) = -\frac{\partial}{\partial x}J(x, t), \quad (10)$$

which is the hydrodynamics limit of equation (1), gives the non-linear partial differential equation

$$\frac{\partial}{\partial t}\varrho(x, t) = -\frac{\partial}{\partial x}\left\{\lambda(x)\varrho(x, t)(1 - \varrho(x, t)) - \nu(x)\frac{\partial}{\partial x}\varrho(x, t)\right\}, \quad (11)$$

which can be linearised to

$$\frac{\partial}{\partial t}u(x, t) = \frac{\tilde{p}(x)}{2}\left\{a^2(1 + b)\frac{\partial^2}{\partial x^2}u(x, t) - \frac{(1 - b)^2}{1 + b}u(x, t)\right\} \quad (12)$$

by means of a generalisation of the Cole-Hopf transform (Appendix A and references [15, 44, 45]). For simplicity we set  $(a, b) = (1, 0)$ , arguing that our considerations remain valid with such a choice. The required boundary values  $\varrho(0, t)$ ,  $\varrho(L, t)$ , and  $\varrho(x, 0)$ , and the numerical scheme used to integrate equation (12) are detailed in Appendices A and B.

Integrating equation (11) with boundary conditions analogous to equations (4)–(5) and initial density  $\varrho(x, 0) > 0$  yields a NESS for large  $t$ , characterised by a non-vanishing average flux and a density profile  $\varrho^*(x)$  which is invariant in time. Setting the latter as initial condition and further integrating with no inward particle flux ( $p_0 = q_N = 0$ ) produces a transient state that mimics the evolution of the PolIII profile after Trp treatment until the density profile vanishes. This is illustrated, for a choice of boundary values and jump rate profile, in Fig. 2, which also includes the result of the inference process described in the next subsections.



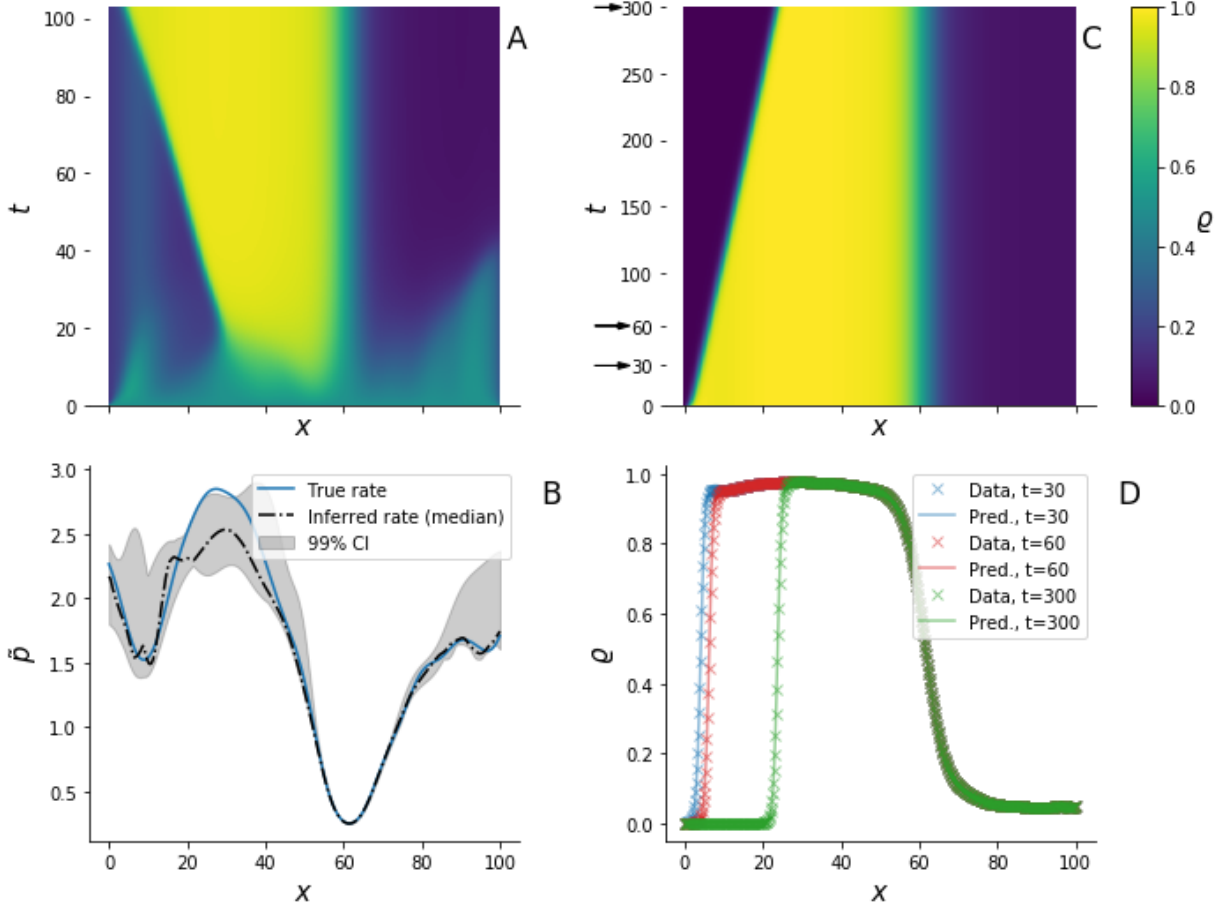


FIG. 2. Simulation study. A) A non-equilibrium stationary state (NESS) of profile  $\varrho^*(x)$  is obtained integrating the hydrodynamic TASEP with open boundaries, initial density profile  $\varrho(x,0) = 0.5 \forall x \in [0, L]$ , and chosen rate profile (solid line in (B)). B) True rate profile (solid line) and inferred rate profile (dash-dot line); the shaded area is 99% credible interval (CI). C) Integrating the same dynamics with initial profile  $\varrho^*(x)$  and no-influx boundary conditions show that the density decreases in proximity of the left-boundary, similar to ChIP-seq readings followed by Trp treatment; the density profiles corresponding to times 30, 60, and 300 and used for inference are marked by arrows. D) The posterior predictive samples (solid lines) are in excellent agreement with the extracted density profiles (cross markers); the posterior predictive dispersion is of the order of the line width, see also Fig. S2.

### C. Bayesian framework

We fit the model to real-world data by means of a Bayesian approach leveraging its ability to explicitly encode prior hypotheses about the quantities we wish to infer [46]. We are interested in the forward rate profile  $\tilde{p}$ . As this is required to be analytic and non-negative, it is convenient to assume a Gaussian process (GP) [16] functional prior on a latent variable  $f$  and induce a prior on  $\tilde{p}$  using a sigmoid link function of  $f$ , such that  $\tilde{p} = \tilde{p}_{\max}/(1 + \exp(-f))$ , which further imposes an upper bound  $\tilde{p}_{\max}$  to  $\tilde{p}$ . The GP prior here defines a distribution over real valued  $C^1$  functions in  $\mathbb{R}$ , where any finite set of function evaluations  $f(x)$  has multivariate normal distribution with mean  $m$  and covariance kernel  $k(x, x'; \sigma_f^2, l) = \sigma_f^2 \exp(-(x - x')^2/(2l^2))$ ,  $x, x' \in \mathbb{R}$ . In practice, the GP is evaluated at the positions  $x_i, i = 1, \dots, n$ , where is it equivalent by definition to  $\mathbf{f} \sim \mathcal{N}(m, \mathbf{K})$ , a multivariate normal random variable with mean  $m$  and covariance matrix  $\mathbf{K}(\sigma_f, l)$  induced by the kernel.

The observations are organised into a collection of values  $\mathbf{y} = \{y_{ij}\}_{i=1,2,\dots,n,j=1,2,\dots,t}$ , where the subscripts indicate that an observation is taken at position  $x_i$  and time  $t_j$ . We assume that the observed values depend on a multiplicative factor and also include an additive error term  $\epsilon \sim \mathcal{N}(0, \sigma_\epsilon)$ . This can be written in terms of the equation  $\kappa y_{ij} = \varrho(x_i, t_j) + \epsilon$ , where  $\kappa$  is the inverse of the amplification factor. The likelihood  $P(\mathbf{y}|\mathbf{f}, \sigma_\epsilon, \kappa)$  satisfies

$$\log P(\mathbf{y}|\mathbf{f}, \sigma_\epsilon, \kappa) = -\frac{1}{2\sigma_\epsilon^2} \sum_{i=1}^n \sum_{j=1}^t (\varrho(x_i, t_j; \mathbf{f}) - \kappa y_{ij})^2 - \frac{n}{2} \log(2\pi\sigma_\epsilon^2), \quad (13)$$

where we made explicit that  $\varrho$  depends on  $\mathbf{f}$ . For the hierarchical parameters  $(m, \sigma_\epsilon, \kappa, \sigma_f, l) =: \theta$  we assume a scaled sigmoid Gaussian prior  $P(m, \sigma_\epsilon, \kappa, \sigma_f, l)$  such that

$$\theta = \theta_{\min} + \frac{(\theta_{\max} - \theta_{\min})}{1 + \exp(-\xi)}, \quad \xi \sim \mathcal{N}(\mu_\xi, \mathbb{1}\sigma_\xi), \quad (14)$$

where  $\theta_{\min} := (m_{\min}, \sigma_{\epsilon\min}, \kappa_{\min}, \sigma_{f\min}, l_{\min})$ ,  $\theta_{\max} := (m_{\max}, \sigma_{\epsilon\max}, \kappa_{\max}, \sigma_{f\max}, l_{\max})$ , and  $(\mu_\xi, \sigma_\xi)$  are referred to as hyperparameters. By virtue of the Bayes theorem the joint posterior probability for  $\theta$  and  $\mathbf{f}$  satisfies

$$P(\mathbf{f}, m, \sigma_\epsilon, \kappa, \sigma_f, l|\mathbf{y}) \propto P(\mathbf{y}|\mathbf{f}, \sigma_\epsilon, \kappa)P(\mathbf{f}|m, \sigma_f, l)P(m)P(\sigma_\epsilon)P(\kappa)P(\sigma_f)P(l), \quad (15)$$

which we draw random samples from by Markov chain Monte Carlo (MCMC) sampling, more specifically block Gibbs sampling with elliptical slice sampling at each block [47, 48] (Appendix C). Equation (15) expresses the distribution of parameters given the observed

data  $\mathbf{y}$  and completes the definition of the model. It is worth noting that evaluating the likelihood also requires computing  $\varrho$  by integrating equation (11) with initial condition  $\varrho(x, 0) = \kappa y^*(x), \forall x \in [0, L]$ .

### III. RESULTS

We first consider simulated data from a given profile of length  $L = 100$  obtained from GP draw with parameters  $(l, \sigma_f, m, \tilde{p}_{\max}) = (7.32, 0.67, 0.29, 3)$ . We integrate the dynamics with NESS initial profile (obtained by fixing the boundary conditions to  $\varrho(0, t) = \varrho(L, t) = 0.5, \forall t$ ) and no-influx boundary conditions (Fig. 2 A-B). The chosen rate profile shows a local minimum close to the left boundary, which yields a minor local perturbation in the density, and a global minimum around  $x \approx 60$ , whose effect propagates along the lattice and acts as a major bottleneck, which separates a low density phase downstream from a high-density phase upstream. These minima correspond to regions where particles slow down or pause for exponentially distributed amount of time. As the particles leave the system through the right boundary and are not replenished by influx through the left boundary, the region upstream the bottleneck is emptied by a reverse wave front.

For the purpose of testing whether we are able to recover the rate profile from time-course observations, we extract density profiles  $\mathbf{y}$  at times  $(t_1, t_2, t_3) = (30, 60, 300)$  and set the hyperparameters  $\theta_{\min}, \theta_{\max}$ , and  $(\mu_\xi, \sigma_\xi)$  to  $(0, 0, 0.8, 0, 0)$ ,  $(2, 10, 1.2, 1, 10)$ , and  $(0, 1)$ , respectively. With these settings and data, we generated  $10^4$  MCMC samples targeting the posterior (15), discarding the first  $2 \times 10^3$  as burn-in. demonstrating that the fitting procedure is able to capture the location of both the major and minor minima of the generative model, as well as the overall elongation rate (Fig. 2 B). It is worth noting that the integrated density profile in Fig. 2 C and D displays a very small effect of the first local minimum (minor dip, captured only by time-course profiles at  $t_1$  and  $t_2$ ); this is reflected in relatively wide credible intervals for the inferred rate profile (grey ribbon in Fig. 2 B). On the other hand, the rate at the bottleneck is inferred with very high confidence. The covariance hyperparameters  $l$  and  $\sigma_f$  control how quickly the rate changes over  $x$ ; these were slightly misestimated to 6.86 (95%CI 4.63–7.16) and 0.76 (95%CI 0.75–0.82), respectively, thus suggesting that increased wobbling in the rate profile is tolerated; minor patterns in the rate profile are in fact smoothed out and are essentially not identifiable in the density profiles obtained

by integration (see Fig. S2). The difficulty of sampling covariance hyperparameters is also addressed, e.g., in [48]. The predicted transient density profiles at  $t = 30, 60, 300$  also are in very good agreement with the input data (Fig. 2 D; in fact, all sampled rate profiles yield similar time-course density profiles despite wide CIs in certain regions (see also Fig. S2).

Applying this method to real-world data requires setting the value of  $\tilde{p}_{\max}$  to an upper limit of prior expectations on the elongation rate. As this has been estimated at around  $2 \times 10^3$  Nt/min in previous studies [24], we set  $\tilde{p}_{\max} = 6 \times 10^3$  Nt/min as an arguably safe upper bound. Literature results can be also used to set bounds on the prior for  $\kappa$ , which regularises the estimation problem [16]. From cultured human cell lines, the total number  $P$  of bound PolIII molecules per cell is estimated to be between  $P_{\min} = 11 \times 10^5$  and  $P_{\max} = 18 \times 10^5$  [49]. This is related to the total number  $Y$  of ChIP-seq counts by  $P = \kappa Y$ . Based on these heuristic considerations, we set  $\kappa_{\min} = P_{\min}/Y$  and  $\kappa_{\max} = P_{\max}/Y$ . All remaining hyperparameters were set identical to the previous simulation experiment.

The results from different genes show a variety of rate profiles which share similar patterns (Fig. 3). The most important observation is that, in all genes considered, the rates vary strongly with the genomic position, with local minima corresponding to regions where PolIIs slow down or pause. In order to look for average patterns, it is desirable to aggregate data from all genes. As genes have different lengths (which in our sample range from 16,680 to 59,880 Nts), we stretch all the rate profiles in the region from TSS+1000 to TES-1000 Nts to the same support length and then average over the genes at each position. This yields the summaries illustrated in Fig. 4 which we refer to as *metagene* rates and are akin to the so-called metagene profiles [50]. Rates are typically lower near the TSS than in the gene body, where elongation approaches its highest rate. The behaviour in proximity of the TES is less definite, with rates varying several fold among the different genes. At the TSS the rate typically dips down consistently with the presence of obstacles that hinder the transport of PolIII. Further downstream in the gene body the rate increases to its highest average value. While the dip is evident in both Spt5 and PolIII results, it is worth noting that upstream the TSS the average rate inferred from PolIII data is higher than that from Spt5. We argue that this difference is due to the fact the former also include poised PolIIs which are not strongly bound to the template and can quickly move towards the TSS before being engaged in transcription. A by-product of the fitting procedure is the estimate of the occupation density  $\varrho(x, t) = \kappa y(x, t)$ , as illustrated in Fig. 2 D for the simulation experiment

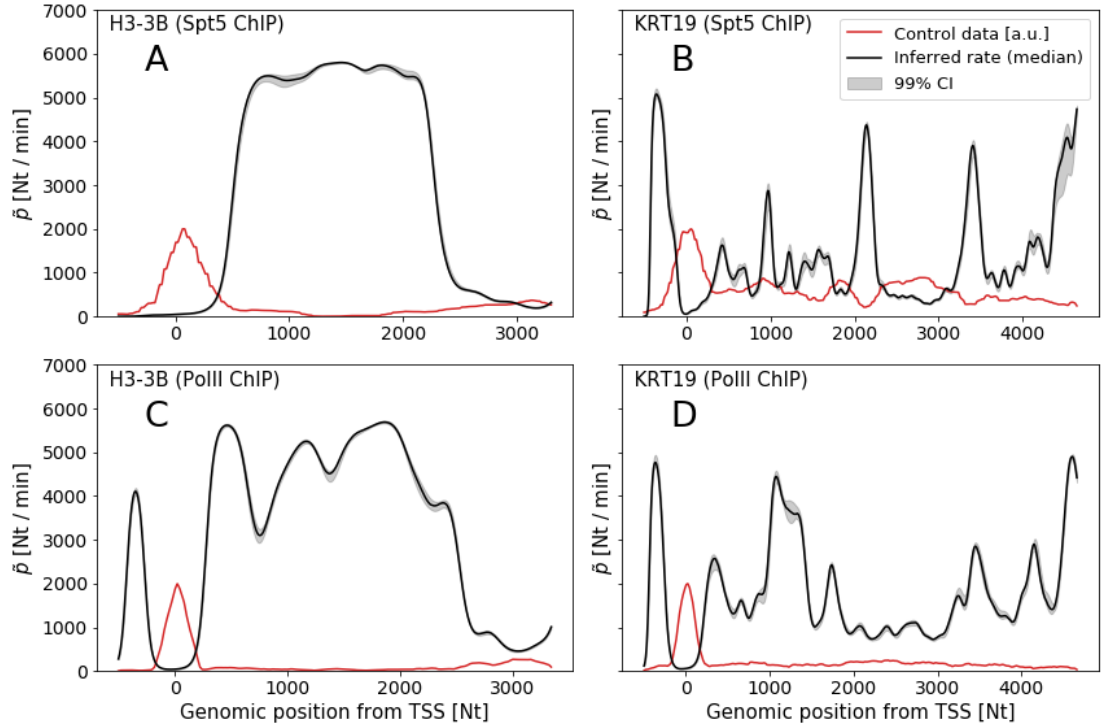


FIG. 3. Inferred rate profiles from Spt5 ChIP-Seq (A-B) and PolII ChIP-Seq (C-D) for genes H3-B3 (A-C) and KRT19 (B-D) (black lines are posterior medians, shaded area are 99% credible intervals), with the latter gene showing a distinctive jagged profiles. Both genes show the lowest rates in proximity of the transcription starting site (TSS). Red lines are unperturbed ChIP-seq signals in arbitrary units (a.u.).

and Figs. 5, S3, S4, and S5 for selected genes. The predicted densities are typically very low (total predicted number of PolIIs in a gene is in the order of  $10^{-1}$ ), thus suggesting that crowding and congestion of PolIIs into a gene might not be substantial even proximal to rate minima.

#### IV. DISCUSSION

We developed a general Bayesian framework to study the dynamics of a one-dimensional transport model given time-resolved density profiles. The general problem addressed here is the identification of the PDE parameters that best describe data as a subset of the true PDE solution (see, e.g., [48, 51–53] and references therein). We focused on the hydrodynamic TASEP with smoothly-varying jump rates (which are the parameters to be inferred) as a

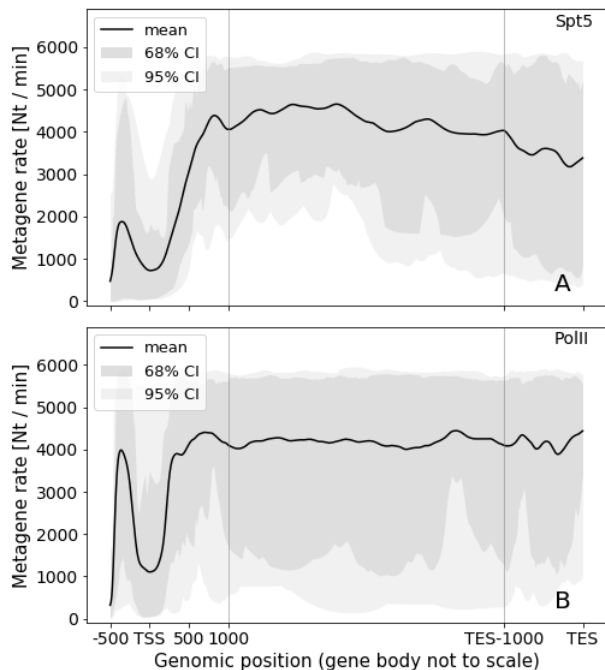


FIG. 4. Metagene rates from PolII ChIP-seq (A) and Spt5 ChIP-seq (B) data. By construction, the metagene analysis conserves the length scale only in proximity of TSS and TES. Upstream of TSS the Spt5 ChIP-seq yields lower average rate than PolII ChIP-seq, as this assay does not detect PolII poised to move downstream.

paradigmatic and well-characterised model of transport. By means of its application to ChIP-seq time-course data, we inferred the rate of PolII elongation as a function of the genomic position in selected genes. This rate is not constant but varies within the gene body. It typically dips down nearby the TSS, confirming widespread pausing in this region, while in the bulk the rate also varies between genes. Low predicted densities suggest that the pausing did not cause congestion or crowding. This is an important observation, as factor crowding has been experimentally observed and associated with regulated gene expression in synthetic and mammalian cell systems [54–58]. Our analysis supports the view that this phenomenon does not happen between PolIIs bound to the gene but it likely occurs elsewhere in the cell.

The inference here is complicated by the high dimensionality of the parameter space (which grows as the genes’ length increases). We addressed this by assuming a Gaussian process latent prior for the jump-rate profile and using elliptic slice sampling as an appropriate MCMC algorithm. The sampling requires multiple evaluations of the likelihood of

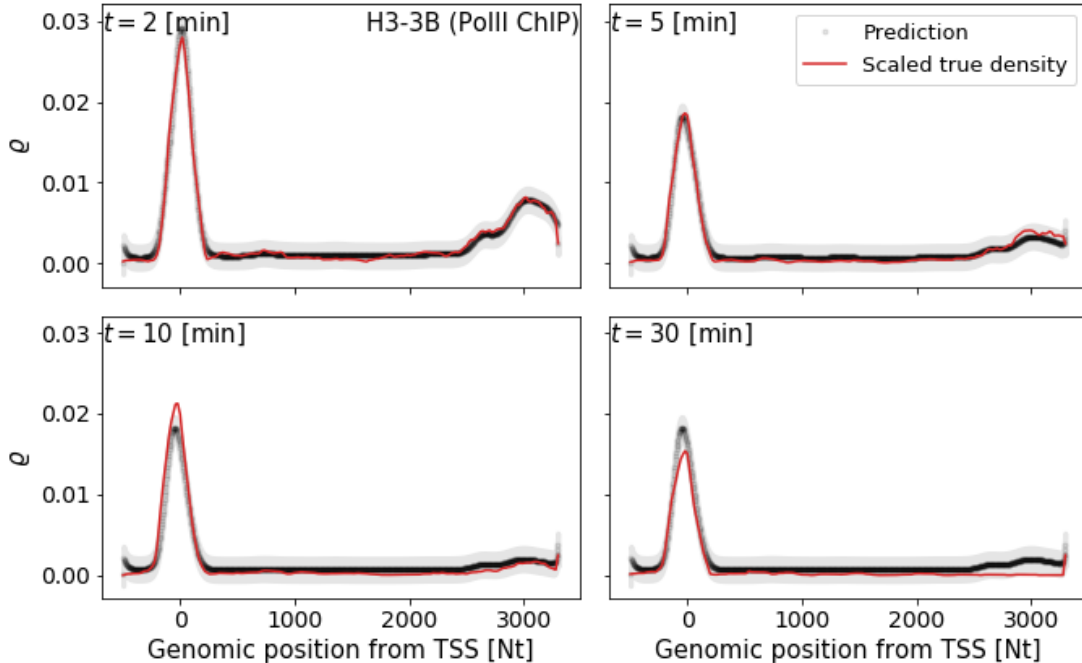


FIG. 5. Predicted density profiles for gene H3-3B from Spt5 ChIP-seq 2, 5, 10, and 20 minutes after Trp treatment as samples from posterior predictive distribution. Grey area is 95% credible interval due to noise model.

equation (13). This in turns requires numerically integrating equation (11), which is also slower in longer genes (require larger integration grids, see Appendix B).

The study of molecular dynamics is also subject to limitations. While ChIP-seq is a widely-used assay to quantify the abundances of DNA-bound PolII, studies suggest that it might be subject to technical issues [59]. Further, the transcription of mRNA is a very complex process and it may be interesting to include features not encoded in the model used for this study. Further TASEP variants, such as those incorporating non-Markovian jump dynamics [60, 61] or Langmuir kinetics [62], are relevant for the modelling of PolII recycling and its early detachment from DNA [58, 63]. Potential extensions also include estimation of the parameters that encode the system's size and asymmetry ( $a$  and  $b$ , respectively) and the boundary values. Nevertheless, including more features arguably comes at the cost of increased computational burden and decreased tractability. Conversely, the chosen TASEP with smoothly-varying jump rates is simple and yet is able to reveal PolII elongation slowing down and speeding up at certain genomic locations. Due to its generality, our approach also serves as a template for future studies seeking to shed light on complex transport phenomena.

## **MATERIALS AND METHODS**

Spt5 and PolII ChIP-seq data mapped to the hg19 University of California at Santa Cruz human genome were downloaded from Gene Expression Omnibus (GEO, <http://www.ncbi.nlm.nih.gov/geo>) accession number GSE117006. We filtered the list of genes from the reference genome to only contain those with unique gene symbols on chromosomes 1–22 and X, thus excluding alternatively spliced genes. Hg19 gene coordinates were flanked 500 Nts upstream the TSS in order to include poised PolII. The 20 non-overlapping genes with the highest coverage of Spt5 ChIP-seq reads were selected. All simulation codes are written in Python (v3.7.1), with the PDE solver using Numba JIT compiler (v0.41.0) [64] (<https://github.com/mcavallaro/dTASEP-fit>).

## **ACKNOWLEDGMENTS**

This research utilised WISB computational facilities (grant ref: BB/M017982/1) funded under the UK Research Councils’ Synthetic Biology for Growth programme. RD is funded by EPSRC (grant nos. EP/V025899/1, EP/T017112/1) and NERC (grant no. NE/T00973X/1). MC acknowledges support from Matt J. Keeling and Health Data Research UK, which is funded by the UK Medical Research Council, EPSRC, Economic and Social Research Council, Department of Health and Social Care (England), Chief Scientist Office of the Scottish Government Health and Social Care Directorates, Health and Social Care Research and Development Division (Welsh Government), Public Health Agency (Northern Ireland), British Heart Foundation and the Wellcome Trust. We thank Carlo Albert and Jie Zhang for valuable comments and the Warwick Bioinformatics RTP for sharing computational resources.

## **AUTHOR CONTRIBUTIONS**

Conceptualization MC DH RD; Data curation MC DH; Formal analysis MC RD; Investigation MC; Software MC YW RD; Writing – original draft MC; Writing – review & editing



- [1] B. Munsky, G. Neuert, and A. van Oudenaarden, *Science* **336**, 183 (2012).
- [2] T. Rajala, A. Häkkinen, S. Healy, O. Yli-Harja, and A. S. Ribeiro, *PLoS Comput. Biol.* **6**, 1 (2010).
- [3] I. Jonkers and J. T. Lis, *Nat. Rev. Mol. Cell Biol.* **16**, 167 (2015).
- [4] A. Mayer, H. M. Landry, and L. S. Churchman, *Curr. Opin. Cell Biol.* **46**, 72 (2017).
- [5] K. Adelman and J. T. Lis, *Nat. Rev. Genet.* **13**, 720 (2012).
- [6] X. Liu, W. L. Kraus, and X. Bai, *Trends Biochem. Sci.* **40**, 516 (2015).
- [7] J. Peccoud and B. Ycart, *Theor. Popul. Biol.* **48**, 222 (1995).
- [8] T. Tripathi and D. Chowdhury, *Phys. Rev. E* **77**, 011921 (2008), 0708.1067.
- [9] M. Dobrzynski and F. J. Bruggeman, *Proc. Natl. Acad. Sci.* **106**, 2583 (2009).
- [10] Z. Cao, T. Filatova, D. A. Oyarzún, and R. Grima, *Biophys. J.* **119**, 1002 (2020).
- [11] J. Szavits-Nossan and R. Grima, *bioRxiv preprint bioRxiv:2022.03.30.486441* (2022), 10.1101/2022.03.30.486441.
- [12] F. Spitzer, *Adv. Math.* **5**, 246 (1970).
- [13] A. Benassi and J.-P. Fouque, *Ann. Probab.* **15**, 546 (1987).
- [14] R. B. Stinchcombe and S. L. De Queiroz, *Phys. Rev. E* **83**, 1 (2011).
- [15] R. J. Harris and R. B. Stinchcombe, *Phys. Rev. E* **70**, 016108 (2004).
- [16] C. E. Rasmussen and C. K. I. Williams, *Gaussian processes for machine learning* (MIT Press, 2006) p. 248.
- [17] C. wa Maina, A. Honkela, F. Matarese, K. Grote, H. G. Stunnenberg, G. Reid, N. D. Lawrence, and M. Rattray, *PLoS Comput. Biol.* **10**, 1 (2014).
- [18] A. Honkela, J. Peltonen, H. Topa, I. Charapitsa, F. Matarese, K. Grote, H. G. Stunnenberg, G. Reid, N. D. Lawrence, and M. Rattray, *Proc. Natl. Acad. Sci.* **112**, 13115 (2015).
- [19] B. Hu, N. Petela, A. Kurze, K.-L. Chan, C. Chapard, and K. Nasmyth, *Nucleic Acids Res.* , gkv670 (2015).
- [20] T. Nojima, T. Gomes, A. R. F. Grosso, H. Kimura, M. J. Dye, S. Dhir, M. Carmo-Fonseca, and N. J. Proudfoot, *Cell* **161**, 526 (2015).
- [21] L. J. Core, J. J. Waterfall, and J. T. Lis, *Science* **322**, 1845 (2008).

- [22] H. Kwak, N. J. Fuda, L. J. Core, and J. T. Lis, *Science* **339**, 950 (2013).
- [23] J. Zhang, M. Cavallaro, and D. Hebenstreit, *Cell Rep. Methods* **1**, 100083 (2021).
- [24] I. Jonkers, H. Kwak, and J. T. Lis, *eLife* **2014**, 1 (2014).
- [25] B. Erickson, R. M. Sheridan, M. Cortazar, and D. L. Bentley, *Genes Dev.* **32**, 1215 (2018).
- [26] T. Chou, K. Mallick, and R. K. P. Zia, *Rep. Prog. Phys.* **74**, 116601 (2011).
- [27] S. Klumpp and T. Hwa, *Proc. Natl. Acad. Sci.* **105**, 18159 (2008).
- [28] J. Cholewa-Waclaw, R. Shah, S. Webb, K. Chhatbar, B. Ramsahoye, O. Pusch, M. Yu, P. Greulich, B. Waclaw, and A. P. Bird, *Proc. Natl. Acad. Sci.* **116**, 14995 (2019).
- [29] T. Tripathi, G. M. Schütz, and D. Chowdhury, *J. Stat. Mech. Theory Exp.* **2009**, P08018 (2009).
- [30] C. T. MacDonald, J. H. Gibbs, and A. C. Pipkin, *Biopolymers* **6**, 1 (1968).
- [31] R. K. P. Zia, J. J. Dong, and B. Schmittmann, *J. Stat. Phys.* **144**, 405 (2011).
- [32] J. Szavits-Nossan, L. Ciandrini, and M. C. Romano, *Phys. Rev. Lett.* **120**, 128101 (2018).
- [33] D. D. Erdmann-Pham, K. Dao Duc, and Y. S. Song, *Cell Syst.* **10**, 183 (2020).
- [34] R. Lipowsky, S. Klumpp, and T. M. Nieuwenhuizen, *Phys. Rev. Lett.* **87**, 108101 (2001).
- [35] D. Chowdhury, L. Santen, and A. Schadschneider, *Physics Reports* **329**, 199 (2000).
- [36] B. Waclaw, J. Cholewa-Waclaw, and P. Greulich, *J. Phys. A: Math. Theor.* **52**, 065002 (2019).
- [37] J. Wang, B. Pfeuty, Q. Thommen, M. C. Romano, and M. Lefranc, *Phys. Rev. E* **90**, 050701 (2014).
- [38] M. Kardar, G. Parisi, and Y. C. Zhang, *Phys. Rev. Lett.* **56**, 889 (1986).
- [39] L. Bertini and G. Giacomin, *Commun. Math. Phys.* **183**, 571 (1997).
- [40] B. Derrida, M. R. Evans, V. Hakim, and V. Pasquier, *J. Phys. A: Math. Gen.* **26**, 1493 (1993).
- [41] A. Lazarescu, *J. Phys. A: Math. Theor.* **48**, 503001 (2015).
- [42] E. Nudler, A. Mustaev, A. Goldfarb, and E. Lukhtanov, *Cell* **89**, 33 (1997).
- [43] F. Jülicher and R. Bruinsma, *Biophys. J.* **74**, 1169 (1998).
- [44] E. Hopf, *Commun. Pure Appl. Math.* **3**, 201 (1950).
- [45] J. D. Cole, *Q. Appl. Math.* **9**, 225 (1951).
- [46] A. Gelman, J. B. Carlin, H. S. Stern, D. B. Dunson, A. Vehtari, and D. B. Rubin, *Bayesian data analysis* (CRC press, 2013).
- [47] I. Murray, R. Adams, and D. MacKay, in *Proceedings of the thirteenth international conference on artificial intelligence and statistics* (JMLR Workshop and Conference Proceedings, 2010)

- pp. 541–548.
- [48] M. Tegnér and S. Roberts, arXiv preprint arXiv:1901.06021 (2019).
  - [49] H. Kimura, Y. Tao, R. G. Roeder, and P. R. Cook, *Mol. Cell. Biol.* **19**, 5383 (1999).
  - [50] C. Joly Beauparlant, F. C. Lamaze, A. Deschênes, R. Samb, A. Lemaçon, P. Belleau, S. Bilodeau, and A. Droit, *PLoS Comput. Biol.* **12**, 1 (2016).
  - [51] S. H. Rudy, S. L. Brunton, J. L. Proctor, and J. N. Kutz, *Sci. Adv.* **3**, e1602614 (2017).
  - [52] M. Raissi, P. Perdikaris, and G. Karniadakis, *Journal of Computational Physics* **378**, 686 (2019).
  - [53] J. Berg and K. Nyström, *Journal of Computational Physics* **384**, 239 (2019).
  - [54] C. Tan, S. Saurabh, M. P. Bruchez, R. Schwartz, and P. Leduc, *Nat. Nanotechnol.* **8**, 602 (2013).
  - [55] D. Hnisz, K. Shrinivas, R. A. Young, A. K. Chakraborty, and P. A. Sharp, *Cell* **169**, 13 (2017).
  - [56] A. J. Plys and R. E. Kingston, *Science* **361**, 329 (2018).
  - [57] A. Boija, I. A. Klein, B. R. Sabari, A. Dall’Agnese, E. L. Coffey, A. V. Zamudio, C. H. Li, K. Shrinivas, J. C. Manteiga, N. M. Hannett, B. J. Abraham, L. K. Afeyan, Y. E. Guo, J. K. Rimel, C. B. Fant, J. Schuijers, T. I. Lee, D. J. Taatjes, and R. A. Young, *Cell* **175**, 1842 (2018).
  - [58] M. Cavallaro, M. D. Walsh, M. Jones, J. Teahan, S. Tiberi, B. Finkenstädt, and D. Hebestreit, *Genome Biol.* **22**, 56 (2021).
  - [59] P. J. Park, *Nat. Rev. Genet.* **10**, 669 (2009).
  - [60] D. Khoromskaia, R. J. Harris, and S. Grosskinsky, *J. Stat. Mech. Theory Exp.* **2014**, P12013 (2014).
  - [61] R. J. Concannon and R. A. Blythe, *Phys. Rev. Lett.* **112**, 050603 (2014).
  - [62] A. Parmeggiani, T. Franosch, and E. Frey, *Phys. Rev. E* **70**, 046101 (2004).
  - [63] B. Steurer, R. C. Janssens, B. Geverts, M. E. Geijer, F. Wienholz, A. F. Theil, J. Chang, S. Dealy, J. Pothof, W. A. van Cappellen, A. B. Houtsmuller, and J. A. Marteiijn, *Proc. Natl. Acad. Sci.* **115**, E4368 (2018).
  - [64] S. K. Lam, A. Pitrou, and S. Seibert, in *Proceedings of the Second Workshop on the LLVM Compiler Infrastructure in HPC - LLVM ’15* (ACM Press, New York, New York, USA, 2015) pp. 1–6.



## Appendix A: Cole-Hopf transform

Let us define a “height” variable  $h(x, t)$  as follows:

$$\varrho(x, t) =: \frac{\partial}{\partial x} h(x, t) + \frac{1}{2}. \quad (\text{A1})$$

Substituting this into equation (11) of the main text yields

$$\frac{\partial}{\partial t} \frac{\partial}{\partial x} h(x, t) = -\frac{\partial}{\partial x} \left\{ \lambda(x) \left( \frac{\partial}{\partial x} h(x, t) + \frac{1}{2} \right) \left( \frac{1}{2} - \frac{\partial}{\partial x} h(x, t) \right) - \nu(x) \frac{\partial^2}{\partial^2 x} h(x, t) \right\} \quad (\text{A2})$$

and integrating over  $x$  gives

$$\frac{\partial}{\partial t} h(x, t) = -\lambda(x) \left( \frac{\partial}{\partial x} h(x, t) + \frac{1}{2} \right) \left( \frac{1}{2} - \frac{\partial}{\partial x} h(x, t) \right) + \nu(x) \frac{\partial^2}{\partial^2 x} h(x, t) + f(t), \quad (\text{A3})$$

which is a noiseless version of the paradigmatic growth model studied by Kardar, Parisi, and Zhang [38] up to an arbitrary integration function  $f(t)$  constant in  $x$ .

This equation is linearised by means of the transformation

$$h(x, t) =: \frac{a}{2} \frac{1+b}{1-b} \ln u(x, t) + F(t), \quad (\text{A4})$$

which obviously implies

$$\frac{\partial}{\partial x} h(x, t) = \frac{a}{2} \frac{1+b}{1-b} \frac{u_x(x, t)}{u(x, t)}. \quad (\text{A5})$$

We refer to  $u(x, t)$  as the “field”.

Merely substituting (A4) into equation (A3) and choosing  $F(t)$  to remove the term  $f(t)$  yields

$$\frac{a}{2} \frac{1+b}{1-b} \frac{u_t(x, t)}{u(x, t)} = - \left\{ \lambda(x) \left[ \frac{1}{4} - \left( \frac{a}{2} \frac{1+b}{1-b} \frac{u_x(x, t)}{u(x, t)} \right)^2 \right] - \nu(x) \frac{a}{2} \frac{1+b}{1-b} \frac{\partial}{\partial x} \frac{u_x(x, t)}{u(x, t)} \right\}, \quad (\text{A6})$$

$$\begin{aligned} \frac{a}{2} \frac{1+b}{1-b} \frac{u_t(x, t)}{u(x, t)} = \\ - a\tilde{p}(x) \left\{ \left[ \frac{(1-b)}{4} - \frac{a^2 (1+b)^2}{4 (1-b)} \frac{(u_x(x, t))^2}{u^2(x, t)} \right] - \frac{a^2 (1+b)^2}{4 (1-b)} \left( \frac{u_{xx}(x, t)}{u(x, t)} - \frac{(u_x(x, t))^2}{u^2(x, t)} \right) \right\}, \end{aligned} \quad (\text{A7})$$

$$\begin{aligned} \frac{1}{2} \frac{1+b}{1-b} \frac{u_t(x, t)}{u(x, t)} = \\ - \tilde{p}(x) \left\{ \frac{(1-b)}{4} - \frac{a^2 (1+b)^2}{4 (1-b)} \frac{(u_x(x, t))^2}{u^2(x, t)} - \frac{a^2 (1+b)^2}{4 (1-b)} \frac{u_{xx}(x, t)}{u(x, t)} + \frac{a^2 (1+b)^2}{4 (1-b)} \frac{(u_x(x, t))^2}{u^2(x, t)} \right\}, \end{aligned} \quad (\text{A8})$$

$$\frac{\partial}{\partial t}u(x, t) = \frac{\tilde{p}(x)}{2} \left\{ a^2(1+b) \frac{\partial^2}{\partial x^2}u(x, t) - \frac{(1-b)^2}{1+b}u(x, t) \right\}, \quad (\text{A9})$$

which, for the totally asymmetric case  $b = 0$ , can be simplified to

$$\frac{\partial}{\partial t}u(x, t) = \frac{\tilde{p}(x)}{2} \left\{ a^2 \frac{\partial^2}{\partial x^2}u(x, t) - u(x, t) \right\}. \quad (\text{A10})$$

To the best of our knowledge, this parametrisation was first derived in reference [15]. If  $\tilde{p}(x) = p$ , it is possible to incorporate a term  $-ap(1-b)t/4$  in  $F(t)$  to eliminate the second term on the right-hand side of equations (A9) and (A10), thus further simplifying these to a diffusion equations.

Equation (A9) preserves the full dynamics of equation (11) of the main text and is linear, thus is easier to treat numerically than the latter. In the next sections we elucidate the numerical scheme for its integration for  $b = 0$ .

We impose Dirichlet boundary conditions for  $\varrho(x, t)$  at  $x = 0$  and  $x = L$ , i.e.,

$$\begin{aligned} \varrho(0, t) &= \varrho_{\text{left}}(t), \\ \varrho(L, t) &= \varrho_{\text{right}}(t), \end{aligned} \quad (\text{A11})$$

$\forall t > 0$ , which implies Neumann conditions for the height  $h(x, t)$ :

$$\begin{aligned} h_x(x, t)|_{x=0} &= \varrho_{\text{left}}(t) - \frac{1}{2}, \\ h_x(x, t)|_{x=L} &= \varrho_{\text{right}}(t) - \frac{1}{2}, \end{aligned} \quad (\text{A12})$$

and Robin (mixed) boundary conditions for the field  $u(x, t)$ :

$$(2\varrho_{\text{left}}(t) - 1)u(0, t)/a - u_x(x, t)|_{x=0} = 0, \quad (\text{A13})$$

$$(2\varrho_{\text{right}}(t) - 1)u(L, t)/a - u_x(x, t)|_{x=L} = 0. \quad (\text{A14})$$

## Appendix B: Numerical integration

The solution  $u^*$  of equation (A10) at the coordinates  $(i \Delta x, j \Delta t)$  is approximated by  $U_{j,i}$  ( $j = 0, 1, \dots, T$  and  $i = 0, 1, \dots, N$  with  $N = L/\Delta x$ ) which is computed using the forward Euler explicit iterative procedure

$$U_{j+1,i} = U_{j,i} + P_i \left[ a^2 \frac{U_{j,i-1} - 2U_{j,i} + U_{j,i+1}}{\Delta x^2} - U_{j,i} \right] \Delta t, \quad (\text{B1})$$

where  $P_i = \tilde{p}(i \Delta x)$ . The approximated density  $\rho_{j,i} \approx \varrho(i \Delta x, j \Delta t)$  is recovered from  $U_{j,i}$  by means of the transformation

$$\begin{aligned} H_{j,i} &= \frac{a}{2} \ln U_{j,i}, \\ \rho_{j,i} &= \frac{1}{2} + \frac{H_{j,i+1} - H_{j,i-1}}{2\Delta x}. \end{aligned} \quad (\text{B2})$$

Initial values  $U_{0,i}$ ,  $i = 0, 1, \dots, \mathbf{N}$ , are obtained by means of the discrete Cole-Hopf transform

$$U_{j,i} = \exp \left( \sum_{k=0}^i \frac{1}{a} (2\rho_{j,k} - 1) \Delta x \right), \quad (\text{B3})$$

at  $j = 0$  and given  $\rho_{0,i}$ . We deal with the boundary conditions by introducing ghost grid points  $(j, -1)$  and  $(j, \mathbf{N} + 1)$ , with  $j = 0, 1, 2, \dots, T$ , where the values of  $U$  are determined according to the procedure detailed below.

We use a central difference formula to approximate the derivatives

$$u_x|_{x=0}(x, t) \approx \frac{U_{j,1} - U_{j,-1}}{2\Delta x}, \quad (\text{B4})$$

$$u_x|_{x=L}(x, t) \approx \frac{U_{j,\mathbf{N}+1} - U_{j,\mathbf{N}-1}}{2\Delta x}, \quad (\text{B5})$$

while  $u(0, t) \approx U_{j,1}$  and  $u(L, t) \approx U_{j,\mathbf{N}}$ . Substituting into equations (A13)–(A14):

$$U_{j,-1} \approx U_{j,1} - 2\Delta x [2\rho_{j,0} - 1] \frac{1}{a} U_{j,0}, \quad (\text{B6})$$

$$U_{j,\mathbf{N}+1} \approx +2\Delta x [2\rho_{j,\mathbf{N}} - 1] \frac{1}{a} U_{j,\mathbf{N}} + U_{j,\mathbf{N}-1}. \quad (\text{B7})$$

The off-grid values  $U_{j,-1}$  and  $U_{j,\mathbf{N}+1}$  correspond to the ghost grid points and are eliminated by substitution from the recursion relations (B1) at  $i = 0$  and  $i = \mathbf{N}$ , which we write for convenience:

$$U_{j+1,0} = U_{j,0} + P_0 \left[ a^2 \frac{U_{j,-1} - 2U_{j,0} + U_{j,1}}{\Delta x^2} - U_{j,0} \right] \Delta t, \quad (\text{B8})$$

$$U_{j+1,\mathbf{N}} = U_{j,\mathbf{N}} + P_{\mathbf{N}} \left[ a^2 \frac{U_{j,\mathbf{N}-1} - 2U_{j,\mathbf{N}} + U_{j,\mathbf{N}+1}}{\Delta x^2} - U_{j,\mathbf{N}} \right] \Delta t. \quad (\text{B9})$$

The approximated second derivatives in the square brackets therefore are

$$\frac{U_{j,-1} - 2U_{j,0} + U_{j,1}}{\Delta x^2} = \frac{L_j U_{j,0} + 2U_{j,1}}{\Delta x^2}, \quad \text{with } L_j = -2 - 2[2\rho_{j,0} - 1]\Delta x \frac{1}{a}, \quad (\text{B10})$$

and

$$\frac{U_{j,\mathbf{N}-1} - 2U_{j,\mathbf{N}} + U_{j,\mathbf{N}+1}}{\Delta x^2} = \frac{2U_{j,\mathbf{N}-1} + R_j U_{j,\mathbf{N}}}{\Delta x^2}, \quad \text{with } R_j = -2 + 2[2\rho_{j,\mathbf{N}} - 1]\Delta x \frac{1}{a}, \quad (\text{B11})$$

for the left and the right boundaries, respectively.

The recruitment of new PolIII at the 5' end of the gene is arrested upon chemical perturbation of the promoters with Trp. This is modelled by assuming that a PolIII molecule at the leftmost site can leave its position, whilst no molecules can be injected. Therefore, in mean-field approximation, the average number of particles at the left boundary of the system obeys

$$\frac{d\phi_0(t)}{dt} = -p_0\phi_0(t)(1 - \phi_1(t)), \quad (\text{B12})$$

whose hydrodynamic limit is approximated by

$$\frac{\partial}{\partial t}\varrho(0, t) \approx -a\tilde{p}(0)\varrho(0, t)(1 - \varrho(0, t) - a\frac{\partial}{\partial x}\varrho(x, t)|_{x=0}^+). \quad (\text{B13})$$

$$(\text{B14})$$

with discretised iterative solution

$$\begin{aligned} \rho_{j+1,0} - \rho_{j,0} &= -\Delta t a P_0 \rho_{j,0} \left( 1 - \rho_{j,0} - a \frac{\rho_{j,1} - \rho_{j,0}}{\Delta x} \right), \\ \rho_{0,0} &= \varrho_L(0), \\ \rho_{0,1} &= \varrho(\Delta x, 0). \end{aligned} \quad (\text{B15})$$

Using equations (B15) to iteratively update  $L_j$  in (B10) yields open boundary conditions, which are used in the simulation experiments.

Sequencing data shows that, at the beginning of the flanked region upstream of the TSS, expression is very low and thus signal will remain constantly close to zero during the time course. The reads downstream the TES are also assumed to be constant within measurement errors, given that the Trp perturbation at the TSS does not propagate up until the TES in the longest time course. Based on this, we set fixed left and right boundary conditions. The grid constants  $\Delta t$  and  $\Delta x$  are chosen such that  $\Delta t/\Delta x^2 = 1/\tilde{p}_{\max}$ , which guarantees numerical stability at each grid point provided that  $\tilde{p}(x) < \tilde{p}_{\max} \forall x \in [0, L]$ . The initial values over this grid at  $j = 0$  are obtained from the binned read profile  $y^*$  by means of linear interpolation.

### Appendix C: MCMC sampling

In equation (15) of the main text, the posterior probability  $P(\mathbf{f}, m, \sigma_\epsilon, \kappa, \sigma_f, l | \mathbf{y})$  is expressed as proportional to the likelihood  $P(\mathbf{y} | \mathbf{f}, \sigma_\epsilon, \kappa)$ , multiplied by the latent GP prior



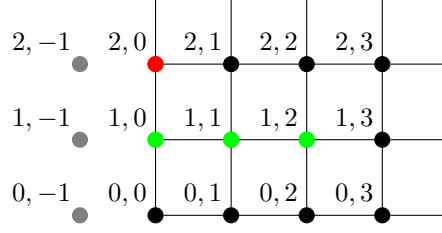


FIG. S1. Evaluation of of the discretised field  $U$  at left-boundary grid nodes. The value at the red node is obtained from the values at the green nodes. Grey points are ghost grid nodes.

$P(\mathbf{f}|m, \sigma_f, l)$  times the prior  $P(m, \sigma_\epsilon, \kappa, \sigma_f, l)$ . To sample from this posterior we used a blocked Gibbs sampling scheme where we recursively update the latent variable  $\mathbf{f}$ , the two covariance variables  $l, \sigma_f$ , and the three likelihood variables  $m, \kappa, \sigma_\epsilon$ , using the so-called elliptic slice sampler [47] for each block.

In order to update  $\mathbf{f}$  as a first block we parametrise the posterior such that  $m$  is absorbed into the likelihood, i.e.,

$$P(\mathbf{f}', m, \sigma_\epsilon, \kappa, \sigma_f, l|\mathbf{y}) \propto P(\mathbf{y}|\mathbf{f}', m, \sigma_\epsilon, \kappa)P(\mathbf{f}'|\sigma_f, l)P(m)P(\sigma_\epsilon)P(\kappa)P(\sigma_f)P(l), \quad (\text{C1})$$

where  $\mathbf{f}' = \mathbf{f} - m$ , and sample from the unnormalised conditional  $P(\mathbf{y}|\mathbf{f}', m, \sigma_\epsilon, \kappa)P(\mathbf{f}'|\sigma_f, l)$  with all hyperparameters  $m, \sigma_\epsilon, \kappa, \sigma_f$ , and  $l$  held fixed.

Updating the second block  $(l, \sigma_f)$  is difficult as this is strongly correlated with  $\mathbf{f}$ . Hence we adopt another parametrisation, which consists of expressing the multivariate Gaussian random variable  $\mathbf{f}'$  as the deterministic function of  $\boldsymbol{\nu}$

$$\mathbf{f}'(\boldsymbol{\nu}, \sigma_f, l) = \mathbf{L}\boldsymbol{\nu}, \quad (\text{C2})$$

where  $\mathbf{L}(\sigma_f, l)$  satisfies  $\mathbf{L}\mathbf{L}^{-1} = \mathbf{K}(\sigma_f, l)$  (it can be computed from  $\mathbf{K}$  using a Cholesky decomposition) and  $\boldsymbol{\nu} \sim \mathcal{N}(0, \mathbb{1})$  is independent of the other variables. This parametrisation incorporates all variables into the likelihood and results in the equivalent posterior

$$P(\boldsymbol{\nu}, m, \sigma_\epsilon, \kappa, \sigma_f, l|\mathbf{y}) \propto P(\mathbf{y}|\mathbf{f}'(\boldsymbol{\nu}, \sigma_f, l), m, \sigma_\epsilon, \kappa)P(\boldsymbol{\nu})P(m)P(\sigma_\epsilon)P(\kappa)P(\sigma_f)P(l). \quad (\text{C3})$$

For a given value of  $(\mathbf{f}', l, \sigma_f)$ ,  $\boldsymbol{\nu}$  is obtained as  $\boldsymbol{\nu} = \mathbf{L}(\sigma_f, l)^{-1} \mathbf{f}'$ . Hence with parameters  $\mathbf{f}', m, \kappa$ , and  $\sigma_\epsilon$  held fixed, we update  $(\sigma_f, l)$  with a sample from the unnormalised conditional  $P(\mathbf{y}|\mathbf{f}'(\boldsymbol{\nu}, \sigma_f, l), \kappa, \sigma_\epsilon)P(\sigma_f)P(l)$ .

In the third step, given the values for  $\mathbf{f}', l$ , and  $\sigma_f$ , the likelihood hyperparameters  $m, \sigma_\epsilon$ , and  $\kappa$  are updated by sampling from the unnormalised conditional  $P(\mathbf{y}|\mathbf{f}', m, \sigma_\epsilon)P(m)P(\sigma_\epsilon)P(\kappa)$ .

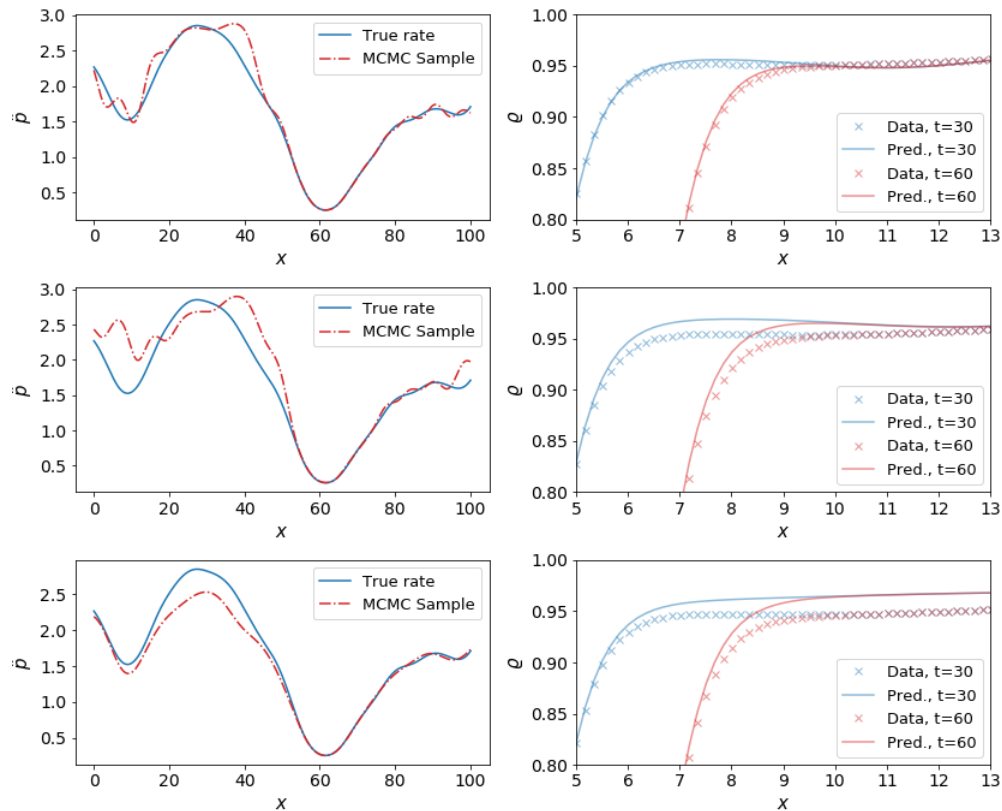


FIG. S2. The rate profile samples sometimes have jagged profiles (left). The resulting density profiles are more smooth than the corresponding rates and their dispersion around the input data profile can be appreciated by zooming in the plot of Fig 2-D (right).

We refer the reader to [48] for more details. Posterior predictions are in very good agreement with time-course observations. Concentration of posterior-predictive samples around target data points can be appreciated by zooming in (Fig. S2). The model is weakly sensitive to changes in the rate profile except for the bottleneck minimum at  $x \approx 60$ , which is sampled with high confidence.

#### Appendix D: Supplemental figures

Figs. S3, S4, and S5 illustrate the posterior predictive samples and the scaled ChIP-seq reads.

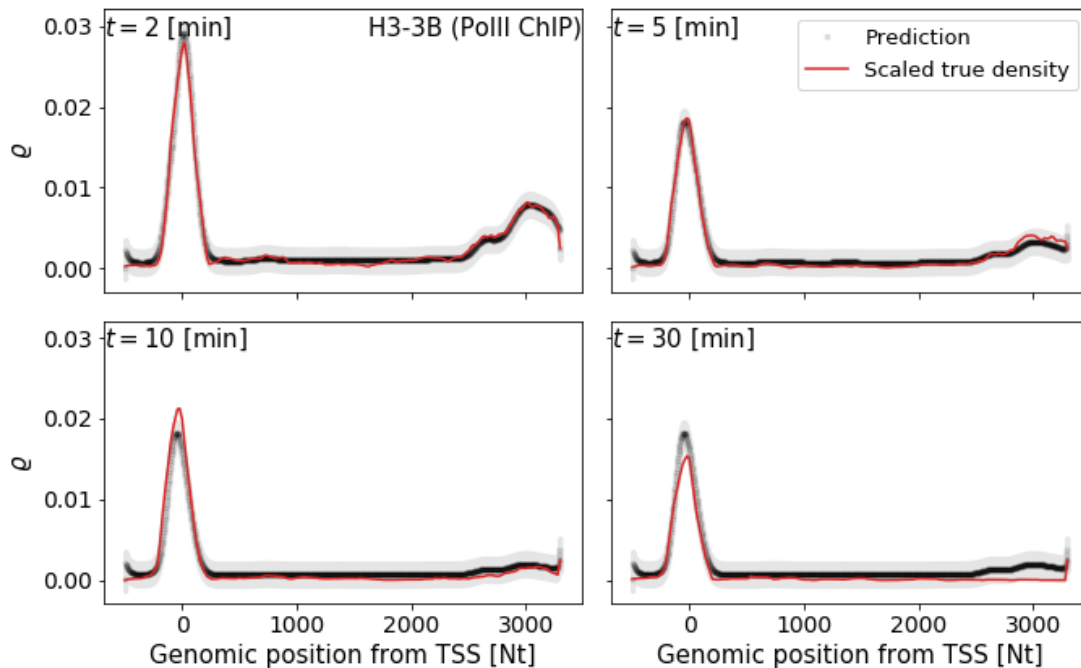


FIG. S3. Predicted density profiles for gene H3-3B from PolII ChIP-seq 2, 5, 10, and 20 minutes after Trp treatment. Markers are posterior predictive samples. Grey area is 95% credible interval due to noise model.

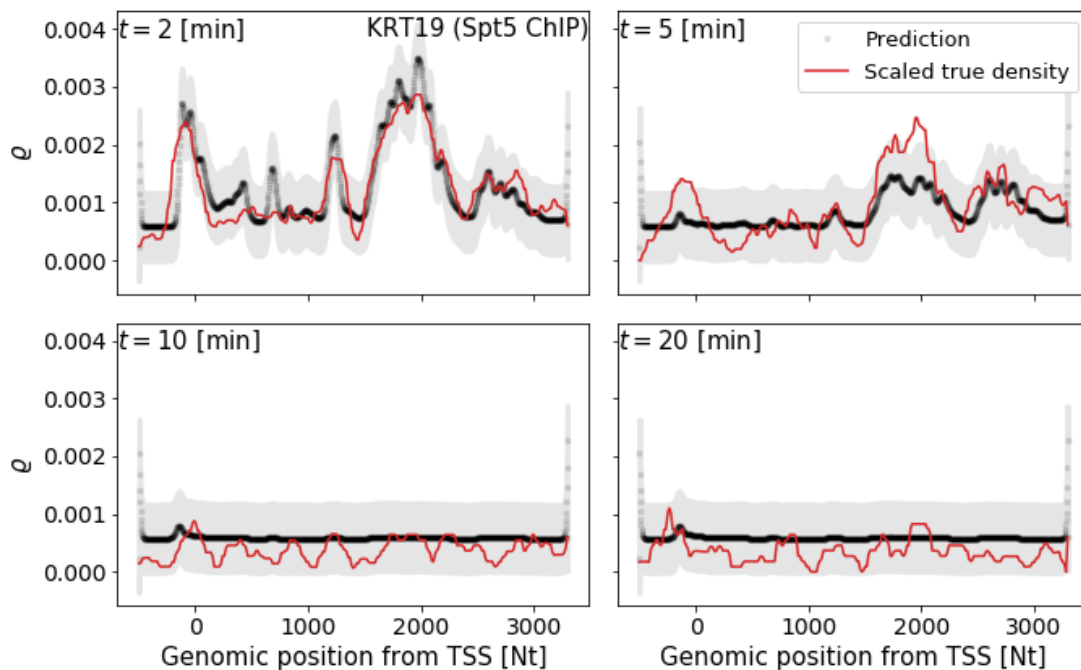


FIG. S4. Predicted density profiles for gene KRT19 from Spt5 ChIP-seq. Figure keys as in Fig. S3.

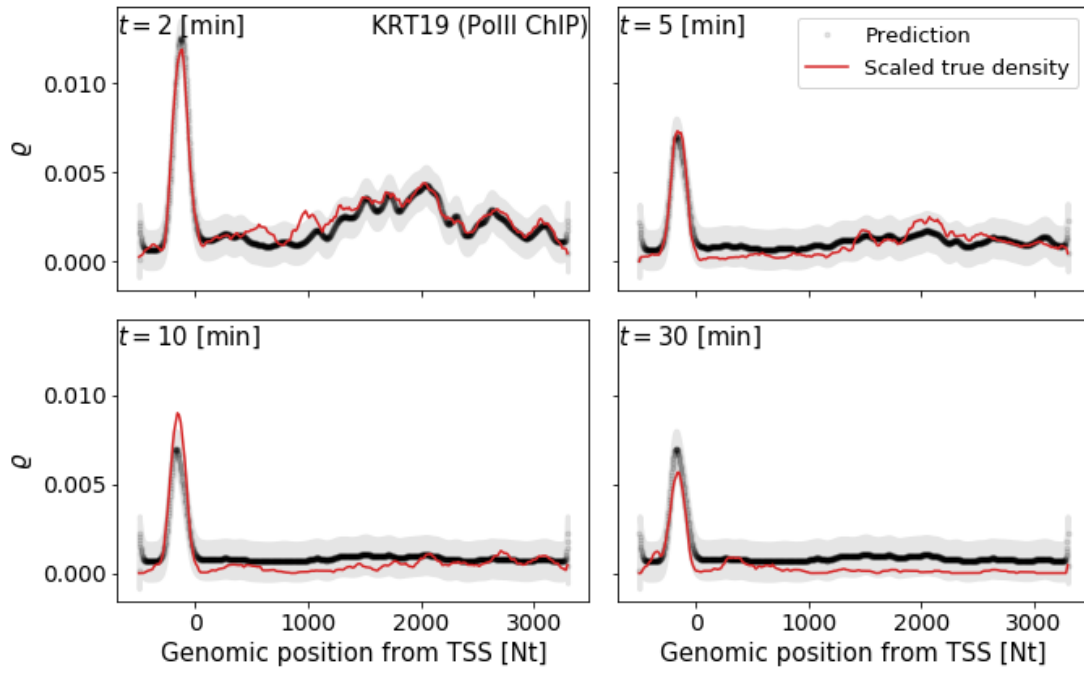


FIG. S5. Predicted density profiles for gene KRT19 from PolIII ChIP-seq. Figure keys as in Fig. S3.